Catalysis Today 153 (2010) 170–175

Contents lists available at ScienceDirect

Catalysis Today

journal homepage: www.elsevier.com/locate/cattod

Complete catalytic oxidation of *o*-xylene over Mn–Ce oxides prepared using a redox-precipitation method

Yinsu Wu, Yuxia Zhang, Min Liu, Zichuan Ma*

College of Chemistry and Material Science, Hebei Normal University, Yuhua East Road 113#, Shijiazhuang 050016, China

ARTICLE INFO

Article history:
Available online 6 March 2010

Keywords:
Mn–Ce oxides
Redox-precipitation method
o-Xylene
Complete catalytic oxidation

ABSTRACT

A series of Mn–Ce oxides were prepared using a redox-precipitation method and the complete catalytic oxidation of *o*-xylene was examined. Catalytic activity was evaluated in terms of both *o*-xylene conversion and CO_2 yield. The effects of the Mn_{at}/Ce_{at} atomic ratio and calcination temperature on the features of catalyst structure and catalytic behavior were examined. When the Mn_{at}/Ce_{at} ratio was 1.5 and the catalyst was calcined at 400 °C, the conversion of *o*-xylene was 100% and the CO_2 yield was 100% at 240 °C. X-ray diffraction (XRD), X-ray fluorescence (XRF), X-ray photoelectron spectroscopy (XPS), and hydrogen temperature-programmed reduction (H_2-TPR) studies revealed that the catalysts prepared via the redox-precipitation method possessed a homogenous dispersion of amorphous MnO_2 and CeO_2 nanoparticles; in the main active phase, MnO_2 provided available oxygen species and CeO_2 enhanced oxygen mobility. The synergistic effects between MnO_2 and CeO_2 potentiated the catalytic activity necessary for the complete catalytic oxidation of *o*-xylene.

1. Introduction

Benzene, toluene, and xylene (BTX) are the major volatile organic compounds (VOCs). They are primarily released during a variety of industrial and commercial processes, such as chemical production, printing, and mobile emission, and cause serious harm to human health. Therefore, the removal of these pollutants is an important research topic for environmental treatment systems [1,2].

Complete catalytic oxidation techniques that convert a contaminant into carbon dioxide (CO_2) and water are an effective way to remove VOCs. Such techniques are advantageous in terms of their high destructive efficiency, low operating temperatures, and low NO_x emissions compared to thermal combustion systems, especially for VOCs at low concentrations [3]. Two types of catalysts can be used, alone or in combination, for oxidizing BTX pollutants: supported noble metals and metal oxides or supported metal oxides. Supported noble metal catalysts, typically Pd and Pt, have been generally preferred for the complete catalytic oxidation of BTX due to their high catalytic activity [4–8]. For instance, complete catalytic oxidation of benzene was achieved at 280 °C over $Pd–V_2O_5/Al_2O_3$ catalysts [5]. Supported Pt or Pt–Pd bimetal catalysts have also demonstrated excellent catalytic activities for the complete catalytic oxidation of benzene, and 100% conversion was reached at 210–250 °C [6]. However, these noble metals are expensive and sometimes show poor thermal stability [9–11]. Kim studied γ-Al_2O_3-supported Cu, Mn, Fe, V, Mo, Co, Ni, and Zn catalysts for the complete catalytic oxidation of benzene, toluene, and xylene. They found that 5 wt% Cu/Al_2O_3 showed the highest catalytic activity among these transition metals, and that 1000 ppm toluene could be completely removed over 5 wt% Cu/Al_2O_3 at 320 °C [9]. Li et al. [10] investigated the complete catalytic oxidation of toluene using Mn–Zn mixed metal oxides prepared via the microemulsion method. Their studies showed that the complete catalytic oxidation of toluene occurred at approximately 220 °C. Alvarez-Merino et al. [11] developed an activated carbon-supported tungsten oxide catalyst for toluene, by which complete catalytic oxidation and 100% toluene conversion were achieved at 300–350 °C. Based on these previously published results, it appears that the catalytic performances of metal oxide catalysts are generally lower than those of noble metal catalysts, despite their higher tolerance for poisons. Moreover, previous studies have primarily focused on BTX conversions without also considering CO_2 yield, which reflects the selectivity of the catalyst for complete catalytic oxidation of BTX. Therefore, it is necessary to develop metal oxide catalysts with higher catalytic activities and selectivity for the complete catalytic oxidation of BTX.

Mn–Ce mixed oxides have been applied as heterogeneous catalysts for the abatement of contaminants in the liquid and gas phases, such as the catalytic reduction of NO and oxidation of acrylic acid and formaldehyde [12–15]. Co-precipitation and sol–gel were the main preparation methods for these Mn–Ce mixed oxides. The

* Corresponding author. Tel.: +86 311 86268343; fax: +86 311 86269217.
E-mail address: ma_zichuan@163.com (Z. Ma).

0920-5861/$ – see front matter © 2010 Elsevier B.V. All rights reserved.
doi:10.1016/j.cattod.2010.01.064

structure and dispersion of Mn–Ce mixed oxides are primarily dependent on the preparation method, which further influences catalytic activity in the abatement of pollutants. Recently, Arena et al. [16–20] reported a new manner of synthesizing Mn–Ce mixed oxides through redox-precipitation reactions using $KMnO_4$, $Mn(NO_3)_2$, and $Ce(NO_3)_3$ as precursors. They devised redox reactions combining MnO_4^- with Ce^{3+} and Mn^{2+} ions in a basic solution to attain the simultaneous precipitation of MnO_2 and CeO_2, which led to a mixture of MnO_2 and CeO_2 species at the atomic level. This new method improved catalyst surface area and caused homogeneous dispersion of the active phase of Mn–Ce oxides; this is in contrast to the conventional co-precipitation method, which typically results in a mixture of monophase hydroxide precipitate particles because of the different precipitation kinetics of the components [16–20]. Moreover, the redox-precipitation were developed for catalytic wet oxidation of organic contaminants in water and showed a superior performance [19,20].

In this study, we investigated the catalytic behavior of Mn–Ce oxide catalysts prepared via the redox-precipitation method and examined the use of these oxides in the complete catalytic oxidation of *o*-xylene. Influencing factors, such as preparation method, Mn/Ce atomic ratio, and calcination temperature, were analyzed.

2. Experimental

2.1. Catalyst preparation

Mn–Ce oxides with varying chemical compositions (Mn_{at}/Ce_{at} = 0.75–3, atomic ratio) were prepared via the redox-precipitation method as described in a previous publication [16]. Each catalyst was denoted as RP-Mn_mCe (*Y*), where *m* is the atomic ratio of Mn_{at}/Ce_{at} and *Y* represents the calcination temperature in °C. For comparison, a Mn–Ce oxide catalyst (Mn_{at}/Ce_{at} = 1) was also prepared via the conventional co-precipitation method. This catalyst was denoted as CP-Mn_1Ce (4 0 0). For detailed procedures, please see Supplementary material.

2.2. Catalyst characterization

Detailed information regarding catalyst characterization using X-ray diffraction (XRD), hydrogen temperature-programmed reduction (H_2-TPR), X-ray photoelectron spectroscopy (XPS), and scanning electron microscopy (SEM) can be found in Supplementary material.

2.3. Catalytic activity measurement

Catalytic activity was measured in a 4-mm i.d. quartz tubular reactor. Approximately 0.25 g of catalyst supported by quartz wool was placed in the middle of the reactor. A gas containing 700 ppm *o*-xylene in simulated air (20 vol.% O_2, 80 vol.% N_2) was continuously passed through the catalyst bed with a flow rate of 50 mL min^{-1} and W/F = 0.30 g s mL^{-1} (corresponding to a GHSV of 8000 h^{-1}). Here, W/F is defined as the catalyst weight divided by the gas flow rate. CO_2 was the only detectable C-containing reaction product, which passed through the TDX-01 stainless steel packed column firstly, and was then converted into methane in a reformer furnace; no significant concentration of any partial oxidation product was detected in the effluents. The reactant and reaction product were analyzed with an online gas chromatograph equipped with two flame ionization detectors (FID) in series. *o*-Xylene conversion ($X_{o\text{-xylene}}$) and the yield of CO_2 (Y_{CO_2}) were calculated according to the following formulas:

$$X_{o\text{-xylene}} = \frac{100 \times (o\text{-xylene}_{in} - o\text{-xylene}_{out})}{o\text{-xylene}_{in}} \quad (1)$$

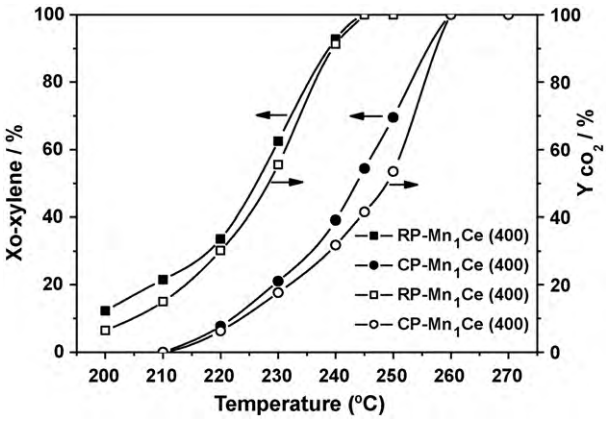

Fig. 1. *o*-Xylene conversion and CO_2 yield over the RP-Mn_1Ce (4 0 0) and CP-Mn_1Ce (4 0 0) catalysts. Reaction conditions: *o*-xylene 700 ppm, 20% O_2/N_2 balance, total flow rate 50 mL min^{-1} and W/F = 0.30 g s mL^{-1}.

$$Y_{CO_2} = \frac{100 \times CO_{2\,out}/8}{o\text{-xylene}_{in}} \quad (2)$$

To ensure that the reactor was isothermal and that diffusion and particle size of the catalysts did not limit the reaction rate, experiments to determine internal and external mass transfer limitations were conducted before the activity measurement. The results are shown in Supporting Information Fig. S1.

3. Results and discussion

3.1. Preparation method effect

The results in Fig. 1 indicate that the temperature dependence of *o*-xylene conversion and CO_2 yield were significantly related to the catalyst preparation method. The RP-Mn_1Ce (4 0 0) catalyst showed a high catalytic activity for the complete oxidation of *o*-xylene, and 100% of *o*-xylene was converted into CO_2 at 245 °C. In contrast, at the same temperature, the CP-Mn_1Ce (4 0 0) catalyst only catalyzed 55% of *o*-xylene, and resulted in a 42% conversion yield into CO_2.

The only C-containing reaction product was CO_2, and no other partial oxidation products were observed in the reactor effluent stream. However, when we compared the $X_{o\text{-xylene}}$ and the Y_{CO_2} at lower temperatures over the two catalysts, we found that the CO_2 yield did not correspond to the *o*-xylene conversion. That is, there was an obvious difference in the carbon balance between *o*-xylene and CO_2 at low reaction temperatures under *o*-xylene oxidation conditions. When the reaction temperature was raised, the difference in the carbon balance gradually disappeared. At 245 and 260 °C, the amount of CO_2 produced was consistent with the amount of *o*-xylene removed over the RP-Mn_1Ce (4 0 0) and CP-Mn_1Ce (4 0 0) samples, respectively. Therefore, it is likely that *o*-xylene, and other undetected by-products, were adsorbed by the catalysts at low temperatures. An increase in the reaction temperature resulted in the desorption and/or reaction of the adsorbed species. This is consistent with previous results [21].

The XRD patterns of the RP-Mn_1Ce (4 0 0) and CP-Mn_1Ce (4 0 0) samples are shown in Supplementary material Fig. S2. The CP-Mn_1Ce (4 0 0) sample exhibited typical diffraction lines for CeO_2 at 2θ = 28.5°, 33.0°, 47.4°, and 56.4° (cerianite, PDF #43-1002), and two very weak peaks at 37.2° and 59.8°, which may be assigned to the incipient crystallization of manganese oxides that were also detected by XRD [14]. For the RP-Mn_1Ce (4 0 0) sample, the XRD pattern consisted of a broad, smooth peak in the 2θ range of 20–40° and another less intense peak in the range of 40–60°. The dominant diffraction peaks for RP-Mn_1Ce (4 0 0) compared to CP-Mn_1Ce (4 0 0) may be primarily attributed to CeO_2 with a low degree of

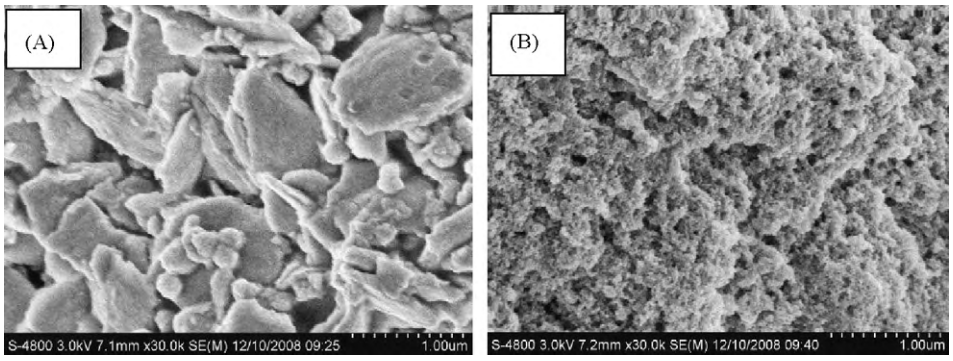

Fig. 2. SEM images of CP-Mn_1Ce (400) (A) and RP-Mn_1Ce (400) (B).

crystallinity and amorphous manganese species that disperse in the microcrystalline CeO_2 [16]. The XRD results indicate that the structure of the RP-Mn_1Ce (400) sample may be incipiently rearranged via the redox-precipitation route.

The BET measurement results show that the surface area and pore volume of RP-Mn_1Ce (400) (93.35 $m^2\,g^{-1}$ and 0.79 $cm^3\,g^{-1}$, respectively) were much larger than those of CP-Mn_1Ce (400) (43.98 $m^2\,g^{-1}$ and 0.19 $cm^3\,g^{-1}$, respectively), which also indicates that the preparation method greatly affects the physical properties of the catalysts.

Further insight into the influence of preparation method on the structural features of the catalysts came from SEM images of the RP-Mn_1Ce (400) and CP-Mn_1Ce (400) samples (Fig. 2A and B). The SEM images show that the texture and morphology of the RP-Mn_1Ce (400) and CP-Mn_1Ce (400) samples differed markedly. The CP-Mn_1Ce (400) sample (Fig. 2A) was made up of large and closely packed particles with irregular morphology. The size of the particles was estimated to be between 200 and 1000 nm. In contrast, the RP-Mn_1Ce (400) sample (Fig. 2B) was more porous and composed of spherical aggregates of nanoparticles (diameter, 30–50 nm) without clear interparticle boundaries. This means that the crystallite growth of MnO_x and CeO_2 in RP-Mn_1Ce (400) can be avoided during the redox reaction process between Mn^{2+}, Ce^{3+}, and MnO_4^-. Furthermore, this findings are consistent with the XRD results; that is, we observed the formation of an amorphous structure that has a high surface area and large pore volume.

The H_2-TPR profiles of RP-Mn1Ce (400) and CP-Mn_1Ce (400) are shown in Supplementary material Fig. S3. The H_2 consumption spectra for these two catalysts can be divided into two different regions that spanned the ranges of 100–550°C (low temperature range, LTR) and 700 – 1000°C (high temperature range, HTR). For CP-Mn_1Ce (400), the spectrum consisted of two resolved H_2 consumption peaks in the LTR centered at 360 and 445 °C, with an onset reduction temperature of 200 °C. The low temperature reduction was attributed to the reduction of MnO_2 to Mn_2O_3, and the high temperature reduction corresponded to the combined reductions of Mn_2O_3 to MnO and surface oxygen removal from CeO_2 in the LTR [14,16,22–24]. In addition, the peak at 1000 °C in the HTR region was attributed to the reduction of CeO_2 to Ce_2O_3 [16]. In contrast, RP-Mn_1Ce (400) showed only one strong H_2 consumption peak at 326 °C in the LTR region, which may be attributable to the reduction of MnO_2 to MnO [16], and the H_2 consumption peak at 445 °C for Mn_2O_3 species reduction was absent. The onset reduction temperature of RP-Mn_1Ce (400) in the LTR region was about 60 °C lower than that of CP-Mn_1Ce (400). Moreover, another less intense HTR H_2 consumption peak emerged at 900 °C, which likely represented the reduction of CeO_2 to Ce_2O_3 [16]; this peak was found about 100 °C lower than in CP-Mn_1Ce (400). TPR analyses show that the redox behaviors of the manganese and cerium oxides in RP-Mn_1Ce (400) were potentiated, indicating an increase in oxygen mobility

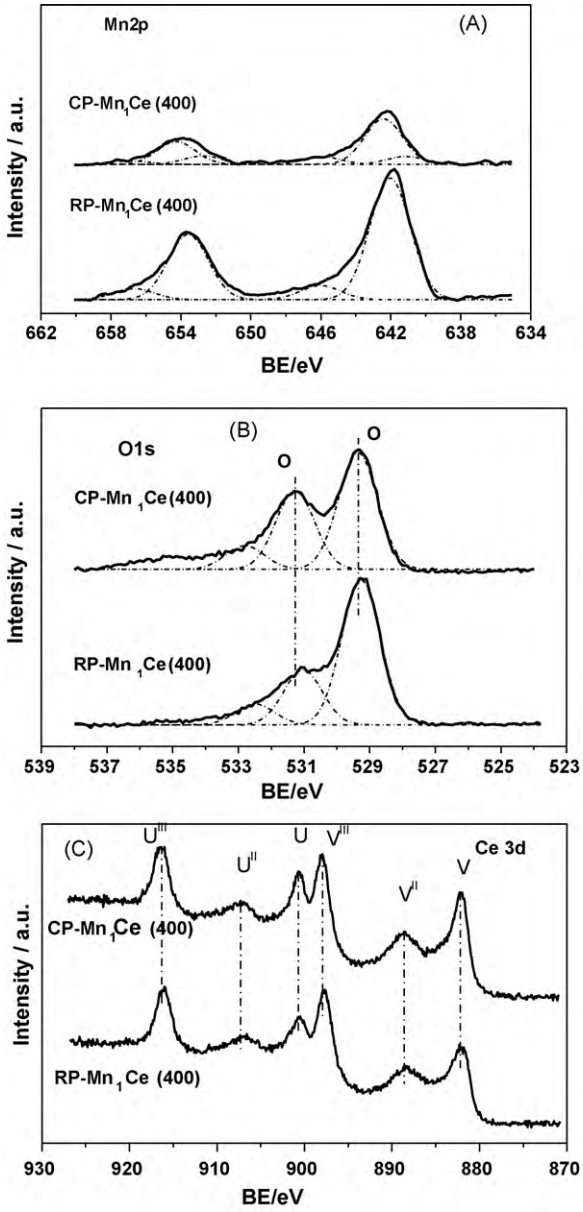

Fig. 3. (A) Mn2p XPS spectra of RP-Mn_1Ce (400) and CP-Mn_1Ce (400) samples. (B) O1s XPS spectra of RP-Mn_1Ce (400) and CP-Mn_1Ce (400) samples. (C) Ce 3d XPS spectra of RP-Mn_1Ce (400) and CP-Mn_1Ce (400) samples.

Table 1
XPS results of RP-Mn1Ce (400) and CP-Mn1Ce (400) samples.

Sample	BE (eV)		$Mn^{4+}/(Mn^{4+}+Mn^{3+})$ (%)	BE (eV)		$O_\alpha/(O_\alpha+O_\beta)$ (%)
	Mn^{4+}	Mn^{3+}		O_α	O_β	
CP-Mn_1Ce (400)	642.4	641.1	82.7	529.4	531.3	59.9
RP-Mn_1Ce (400)	642.1	0	100	529.3	531.1	72.5

and availability. This result shows that synergistic effects occurred between the manganese and cerium oxides in the RP-Mn_1Ce (400) sample. Therefore, we deduced that MnO_2 is the active species for the oxidation of *o*-xylene, and that CeO_2 acts as a transporter that enhances the oxygen mobility of the catalyst. The H_2-TPR results also suggest that the preparation method plays an important role in the redox behavior of these Mn–Ce oxides.

The RP-Mn_1Ce (400) and CP-Mn_1Ce (400) samples were also examined via XPS to determine the oxidation state and surface atomic concentration of manganese oxides. Fig. 3(A) shows the spectra of Mn2p in the RP-Mn_1Ce (400) and CP-Mn_1Ce (400) samples. The XPS spectrum of RP-Mn_1Ce (400) showed a strong Mn2p peak at 642.1 eV, which is consistent with the reported range of 641.1–642.4 eV for MnO_2 in a previous study [25], and indicates that MnO_2 species formed on the RP-Mn_1Ce (400) sample. The sharpening of XPS peak intensity may be attributed to the stabilization of only one type of manganese oxide [26]. One possible explanation is that $KMnO_4$, which is a powerful oxidant, caused the spontaneous formation of MnO_2 nanoparticles by reacting with $Mn(NO_3)_2$ in the basic solution. Furthermore, the intense signal at 642.1 eV indicates that there was a high surface atomic concentration of Mn in the RP-Mn_1Ce (400) sample. In the case of the CP-Mn_1Ce (400) sample, the XPS peak for Mn2p appeared to be broad and less intense than in the RP-Mn_1Ce (400) sample, which suggests that MnO_x exists in more than one oxidation state and that the surface atomic concentration of Mn is low [26–28]. TPR analyses also indicated the presence of two kinds of manganese oxide in the CP-Mn_1Ce (400) sample. The presence of satellite peaks at 646.0–647.0 eV likely originated from the charge transfer between the outer electron shell of the ligand and the unfilled 3d shell of Mn during the creation of the core–hole in the photoelectron process [29]. Table 1 lists the surface compositions of Mn^{4+} in the RP-Mn_1Ce (400) and CP-Mn_1Ce (400) samples, which were calculated based on their respective XPS spectra. According to the XPS calculation, the RP-Mn_1Ce (400) and CP-Mn_1Ce (400) samples possessed 100 and 82.7% Mn^{4+}, respectively. Thus, the large amount of Mn^{4+} species on the surface of the RP-Mn_1Ce (400) catalyst may account for the high activity and selectivity of this catalyst during the complete catalytic oxidation of *o*-xylene.

The XPS spectra for O1s in the RP-Mn_1Ce (400) and CP-Mn_1Ce (400) samples are shown in Fig. 3(B), and two types of oxygen species were clearly distinguished through deconvolution of the spectra. A binding energy of 529–530 eV was ascribed to the lattice oxygen (O^{2-}; denoted as O_α) [14] and the higher binding energy peak around 531–532 eV was ascribed to defective oxides or surface oxygen ions with low coordination (denoted as O_β) [14]. Table 1 shows that the O_α contents were 72.5 and 59.9% for the RP-Mn_1Ce (400) and CP-Mn_1Ce (400) samples, respectively. Obviously, the RP-Mn_1Ce (400) sample possessed more lattice oxygen species than the CP-Mn_1Ce (400) sample, confirming that there was enhanced mobility and availability of lattice oxygen species due to the synergistic effects of MnO_2 and CeO_2 in RP-Mn_1Ce (400). These results from the O1s XPS spectrum for RP-Mn_1Ce (400) are consistent with the results of our TPR analysis. We deduced that O_α is the main active oxygen species and is responsible for the high catalytic activity of RP-Mn_1Ce (400) in the complete oxidation of *o*-xylene.

Fig. 3(C) represents the XPS spectra of Ce3d in the RP-Mn_1Ce (400) and CP-Mn_1Ce (400) samples. The spectra were deconvolved into two spin-orbit, and letters U and V refer to the $3d_{3/2}$ and $3d_{5/2}$ spin–orbit components respectively. All the peaks V, V^{II}, V^{III}, U, U^{II} and U^{III} were attributed to Ce^{4+} [30].

To evaluate the effect of preparation method on the dispersion of Mn on the catalyst surface and in bulk, the surface and bulk Mn/Ce atomic ratios (Mn2P/Ce3d) were calculated based on the XPS and X-ray fluorescence (XRF) data, respectively. These results are given in Table 2. For RP-Mn_1Ce (400), the Mn/Ce surface value (1.3) was similar to the bulk atomic composition (1.2). This result demonstrates that MnO_2 and CeO_2 are homogeneously dispersed in the RP-Mn_1Ce (400) sample. However, in the CP-Mn_1Ce (400) sample, the surface Mn/Ce value was threefold lower than the bulk atomic composition, indicating a much lower surface dispersion of the active phase Mn ions in CP-Mn_1Ce (400). These results suggest that the homogeneous dispersion of the Mn^{4+} and Ce^{4+} ions in the RP-Mn_1Ce (400) sample plays an important role in *o*-xylene catalytic oxidation.

3.2. *Effect of the Mn_{at}/Ce_{at} atomic ratios*

The conversion of *o*-xylene and the CO_2 yield over RP-MnCe (400) samples with Mn_{at}/Ce_{at} = 0.75–3 calcined at 400 °C is shown in Fig. 4. As the manganese content of the samples increased from 0.75 to 1, the conversion of *o*-xylene and the CO_2 yield increased significantly. Although the samples of Mn_{at}/Ce_{at} = 1–2 exhibited similar high catalytic activities for *o*-xylene removal, the optimum Mn_{at}/Ce_{at} ratio was 1.5, at which 100% conversion of *o*-xylene was achieved at 240 °C. However, the catalytic activity of the sample with Mn_{at}/Ce_{at} = 3 decreased slightly. These results suggest that the catalytic activities of the samples depend on an appropriate Mn_{at}/Ce_{at} ratio and high dispersion on the catalyst. Catalysts with the highest and lowest CeO_2 contents (Mn_{at}/Ce_{at} = 0.75 and Mn_{at}/Ce_{at} = 3) exhibited lower catalytic activities because of the low MnO_2 content or poor dispersion of the MnO_2 active phase and CeO_2 on the catalyst surface. Furthermore, the samples with appropriate Mn_{at}/Ce_{at} ratios (between 1 and 2) exhibited the highest activities for *o*-xylene complete catalytic oxidation due to the high dispersion of MnO_2 and CeO_2.

The XRD patterns of the RP-$Mn_{0.75-3}$Ce (400) samples are presented in Supplementary material Fig. S4. All RP-MnCe (400) samples showed similar XRD patterns consisting of a broad, smooth peak in the 2θ range of 20–40° and a less intense peak within the range of 40–60°. As discussed above, these broad patterns may be

Table 2
The surface and bulk Mn/Ce atomic ratio of the sample.

Sample	Composition (wt%, XRF)	Atomic ratio of Mn/Ce	
		XRF	XPS[a]
CP-Mn_1Ce (400)	MnO – 30.5 CeO_2 – 64.9 Others – 4.6	1.1	0.4
RP-Mn_1Ce (400)	MnO – 30.3 CeO_2 – 63.3 Others – 6.4	1.2	1.3

[a] Surface manganese-to-cerium atomic ratio from Mn2P/Ce3d signals.

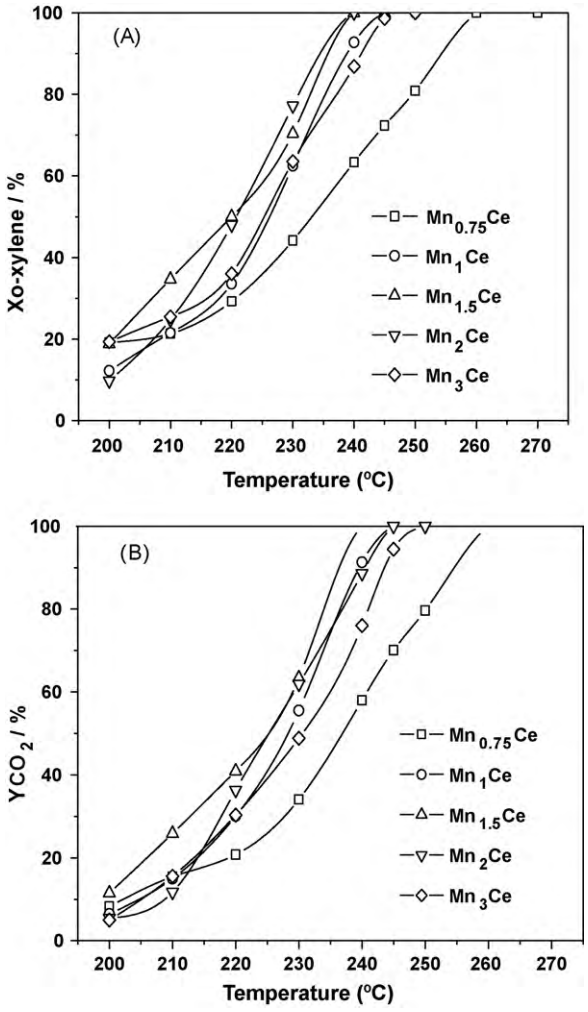

Fig. 4. Effect of Mn_{at}/Ce_{at} atomic ratio on *o*-xylene conversion (A) and CO_2 yield (B) over RP-MnCe (4 0 0) samples. Reaction conditions: *o*-xylene 700 ppm, 20% O_2/N_2 balance, total flow rate 50 mL min^{-1}, W/F = 0.30 g s mL^{-1}.

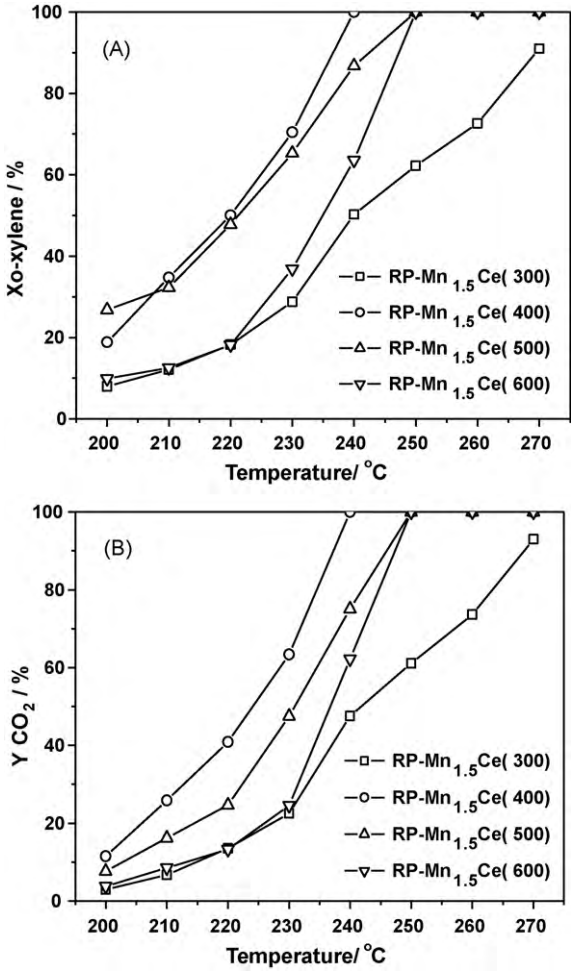

Fig. 5. Effect of calcination temperature on *o*-xylene conversion (A) and CO_2 yield into (B) over the RP-$Mn_{1.5}$Ce samples. Reaction conditions: *o*-xylene 700 ppm, 20% O_2/N_2 balance, total flow rate 50 mL min^{-1}, W/F = 0.30 g s mL^{-1}.

attributable to a microcrystalline CeO_2 structure with the amorphous MnO_2 active phase dispersed throughout. Based on these observations, these atypical diffraction patterns from RP-MnCe (4 0 0) samples may be attributable to the lack of a long-range crystalline order, according to the characteristics of the synthetic route, and may be due to a very intimate adhesion of the MnO_2 and CeO_2 molecules that hinders the growth of large crystalline domains during synthesis [16]. Although all RP-MnCe (4 0 0) samples showed similar XRD patterns, a systematic decrease in the intensity, along with an increase in the Mn_{at}/Ce_{at} ratio, was noted in Fig. S4. This suggests that these peaks are mostly related to the CeO_2 content.

3.3. Effect of calcination temperature

Because calcination of the catalyst leads to structural changes that further influence catalytic activity, we examined the effect of calcination temperature on the catalytic activity of RP-$Mn_{1.5}$Ce samples during the catalytic oxidation of *o*-xylene. The activities of RP-$Mn_{1.5}$Ce catalysts that were calcined at 300–600 °C are shown in Fig. 5. *o*-Xylene conversion and CO_2 yield increased significantly as the calcination temperature increased from 300 to 400°C; thereafter, catalytic activity decreased gradually as calcination temperature increased. The temperature for 100% conversion of *o*-xylene and 100% CO_2 yield increased from 240 to 260 °C when the calcination temperature increased from 400 to 600 °C.

The phase structures of RP-$Mn_{1.5}$Ce catalysts calcined at different temperatures were analyzed by XRD and the results are shown in Supplementary material Fig. S5. As discussed above, the XRD pattern of RP-$Mn_{1.5}$Ce showed two broad peaks in the 2θ range of 20–40° and 40–60° below 400°C. These peaks may be primarily attributable to CeO_2, which has a low degree of crystallinity. When the catalyst was heated to 500 °C, the broad peaks became intense in the XRD pattern, with sharp diffractions at 2θ = 28.7°, 33.3°, 47.7°, and 56.2°, indicating that the crystals of the CeO_2 oxide species became larger. When the sample was further heated to 600 °C, CeO_2 became the dominant phase together with a trace amount of crystalline MnO_2. The phase separation of CeO_2 resulted in the loss of the synergistic effects between MnO_2 and CeO_2, and further decreased catalytic activity. Therefore, the sintering of catalysts plays a major role in the deactivation of the RP-$Mn_{1.5}$Ce samples during calcination. As for the RP-$Mn_{1.5}$Ce (300) sample, the lower catalytic activity may indicate that the active site was not activated when the sample calcined at 300 °C, although it showed a similar XRD pattern compared to RP-$Mn_{1.5}$Ce (4 0 0).

3.4. Stability test for the RP-$Mn_{1.5}$Ce catalyst

In the isothermal combustion of *o*-xylene at 240 °C for 60 h over RP-$Mn_{1.5}$Ce (shown in Fig. S6), the CO_2 yield remained >98% for the duration of the test. This result indicates that RP-$Mn_{1.5}$Ce is relatively stable under these working conditions.

4. Conclusion

Mn–Ce oxides prepared via the redox-precipitation method and calcined at 400 °C exhibited much higher catalytic activities for the complete catalytic oxidation of *o*-xylene compared to catalysts prepared via the conventional co-precipitation method. RP-MnCe (400) catalysts with a Mn_{at}/Ce_{at} ratio between 1 and 2 resulted in a high MnO_2 content and dispersion. At 240 °C, 100% *o*-xylene conversion and 100% CO_2 yield were achieved. XRD, TPR, XRF, and XPS analyses revealed that amorphous MnO_2, which is dispersed among microcrystalline CeO_2, served as the active phase. MnO_2 provided oxygen species availability, while CeO_2 enhanced the oxygen mobility. The synergistic effects between MnO_2 and CeO_2 promoted redox behavior and played an important role in the complete catalytic oxidation of *o*-xylene.

Acknowledgements

The author appreciates the valuable discussion with Prof. Hong He and experimental help from his research group in RCEES, Chinese Academy of Sciences.

This research is supported by the National Natural Science Foundation of China (No. 20977024), the Natural Science Foundation of Hebei Province (No. B2009000258), the Natural Science Foundation of Hebei Education Department (No. 2008128) and Doctoral Foundation of Hebei Normal University (No. L2005B16).

Appendix A. Supplementary data

Supplementary data associated with this article can be found, in the online version, at doi:10.1016/j.cattod.2010.01.064.

References

[1] J. Spivey, Ind. Eng. Chem. Res. 26 (1987) 2165.
[2] A. Jones, Atmos. Environ. 33 (1999) 4535.
[3] C. Lahousse, A. Bernier, P. Grange, B. Delomn, P. Papaefthimiou, T. Ioannides, X. Verykios, J. Catal. 178 (1998) 214.
[4] H.L. Tidahy, S. Siffert, F. Wyrwalski, J.F. Lamonier, A. Aboukĭs, Catal. Today 119 (2007) 317.
[5] R.S.G. Ferreira, P.G.P. de Oliveira, F.B. Noronha, Appl. Catal. B 50 (2004) 243.
[6] H. Kim, T. Kim, H. Koh, S. Lee, B. Min, Appl. Catal. A 280 (2005) 125.
[7] J. Li, X. Xu, Z. Jiang, Z. Hao, C. Hu, Environ. Sci. Technol. 39 (2005) 1319.
[8] T. Garcia, B. Solsona, D. Cazorla-Amoroïs, A. Linares-Solano, S.H. Taylor, Appl. Catal. B 62 (2006) 66.
[9] S.C. Kim, J. Hazard. Mater. B 91 (2002) 285.
[10] W.B. Li, W.B. Chu, M. Zhuang, J. Hua, Catal. Today 93–95 (2004) 205.
[11] M.A. Alvarez-Merino, M.F. Ribeiro, J.M. Silva, F. Carrasco-Marín, F.J. Maldonnado-Hodar, Environ. Sci. Technol. 38 (2004) 4664.
[12] G. Qi, R.T. Yang, R. Chang, Appl. Catal. B 51 (2004) 93.
[13] G. Qi, R.T. Yang, J. Catal. 217 (2003) 434.
[14] X. Tang, Y. Li, X. Huang, Y. Xu, H. Zhu, J. Wang, W. Shen, Appl. Catal. B 62 (2006) 265.
[15] A.M.T. Silva, R.R.N. Marques, M. Quinta-Ferreira, Appl. Catal. B 47 (2004) 269.
[16] F. Arena, G. Trunfio, J. Negro, B. Fazio, L. Spadaro, Chem. Mater. 19 (2007) 2269.
[17] F. Arena, J. Negro, A. Parmaliana, L. Spadaro, G. Trunfio, Ind. Eng. Chem. Res. 46 (2007) 6724.
[18] F. Arena, G. Trunfio, J. Negro, L. Spadaro, Appl. Catal. B 85 (2008) 40.
[19] F. Arena, G. Trunfio, J. Negro, L. Spadaro, Mater. Res. Bull. 43 (2008) 539.
[20] F. Arena, G. Trunfio, B. Fazio, J. Negro, L. Spadaro, J. Phys. Chem. C 113 (2009) 2822.
[21] P. Papaefthimiou, T. Ioannides, X.E. Verykios, Appl. Catal. B 13 (1997) 175.
[22] F. Kapteijn, L. Singoredjo, A. Andreini, Appl. Catal. B 3 (1994) 173.
[23] A. Trovarelli, Catal. Rev. Sci. Eng. 38 (1996) 439.
[24] J. Carnö, M. Ferrandon, E. Björbom, S. Järås, Appl. Catal. A 155 (1997) 265.
[25] M. Ferrandon, J. Carnö, S. Järas, E. Björnbom, Appl. Catal. A 180 (1999) 141.
[26] P.R. Ettireddy, N. Ettireddy, S. Mamedov, P. Boolchand, P.G. Smirniotis, Appl. Catal. B 76 (2007) 123.
[27] A. Wöllner, F. Lange, J. Schmelz, H. Knözinger, Appl. Catal. A: Gen. 94 (1993) 181.
[28] M.C. Álvarez-Galván, V.A. O' Shea, J.L.G.F. ierro, P.L. Arias, Catal. Commun. 4 (2003) 223.
[29] M. Kang, E.D. Park, J.M. Kim, J.E. Yie, Appl. Catal. A 327 (2007) 261.
[30] D.R. Mullins, S.H. Overbury, D.R. Hunteley, Surf. Sci. 409 (1998) 307.